Effect of a non-hydrostatic core-mantle boundary on the nutations of Mars

Marta Folgueira López[1], Véronique Dehant[2,3], Mihaela Puica[4], Tim Van Hoolst[2]

[1]Department Physics of the Earth and Astrophysics, Faculty of Mathematical Sciences, Plaza de Ciencias 3. Universidad Complutense de Madrid, Madrid, 28040, Spain
[2]Service Reference frames and planetology, Royal Observatory of Belgium, Brussels, 1180, Belgium
[3]Earth and Life Institute (ELI), Université catholique de Louvain (UCLouvain), Louvain-la-Neuve, 1348, Belgium
[4]Department of Mathematics, University of Oslo, Oslo, NO-0316, Norway

Correspondence to: Marta Folgueira (martafl@mat.ucm.es)

Abstract. Dynamic loads in planetary mantles have the potential to deform the core-mantle boundary (CMB). On Earth, subducting slabs primarily induce a degree 2–order 2 deformation of the CMB in the spherical harmonic (SH) reference system. On Mars, the presence of the dichotomy and of the Tharsis region could produce loading across multiple degrees and orders, including degree-1, degree 2–order 2, degree 2–order 0, and degree 3–order 3 components. Thanks to the InSight (Interior exploration using Seismic Investigations, Geodesy, and Heat Transport) mission's radio science experiment, observations of Mars' nutations are now available. Periodic length-of-day (LOD) variations of Mars have been detected first by radio tracking the Viking landers, and InSight data have indicated the presence of a secular trend in LOD. In the case of nutations, the Martian core's non-hydrostatic flattening plays a first-order role in determining nutation amplitudes. In this study, we explore second-order effects arising from dynamic topography at the CMB. We compute the pressure exerted on the CMB topography inside Mars' liquid core and evaluate the resulting topographic pressure torque acting on the boundary, which can influence both nutations and LOD variations. Our results show that, albeit at microarcsecond level—well below current observational thresholds, the most significant contribution to nutations arises from degree 2–order 2 component. As for LOD variations, while Earth exhibits notable contributions from inertial wave resonances, the situation on Mars is different. The planet's tidal LOD variations have periods that are either too long or too far apart from those of inertial waves. Consequently, the associated contributions fall below the level of detectability.

Introduction

Thanks to the RISE (Rotation and Interior Structure Experiment) radio science experiment, part of NASA's InSight mission (Interior Exploration using Seismic Investigations, Geodesy, and Heat Transport), Mars' rotation and spatial orientation can now be determined with high precision. In particular, variations in the Length-of-Day (LOD) have been measured with an accuracy of 0.002 milliseconds (equivalent to 2 milliarcseconds (mas)), and nutations have been resolved to within a few milliarcseconds (Le Maistre et al., 2023). The nutation data confirm that Mars' core is at least partially liquid.

The nutation of Mars is mainly induced by the Sun, since its moons Phobos and Deimos are very small, and their tidal effects remain weak (Baland et al., 2020). Consequently, the dominant nutation frequencies are the annual term and its sub-harmonics (semi-annual, ter-annual, quarter-annual, etc.). The annual term corresponds to one Martian year (about 1.88 Earth years, i.e. 687 days). Their amplitudes reach more than 500 mas in the prograde frequency band and more than 130 mas in the retrograde frequency band. These nutations are particularly valuable because they provide constraints on the interior structure of Mars, especially the size and state of its core (Dehant et al., 2000, 2009, 2011, 2012; Le Maistre et al., 2023). In addition, a nutation of about 5 mas amplitude with a period of 826 days has been identified, arising from a combination of terms involving both the orbital period of Phobos and the orbital motion of Mars.

Seasonal variations in Mars' length of day (LOD) are substantial because a significant fraction of the atmosphere—about one quarter—participates in the sublimation and condensation cycle at the polar ice caps. Remarkably, these variations are comparable in magnitude to those on Earth, despite Mars having a much thinner atmosphere.

The internal structure of the Martian mantle has been inferred from seismic data (Banerdt et al., 2020; Drilleau et al., 2021, 2025; Stähler et al., 2021; Khan et al., 2021; Samuel et al., 2024) and spacecraft-derived gravity field measurements (e.g., Konopliv et al., 2016). These observations provide evidence for subsurface mass anomalies, associated viscous relaxation, and dynamic topography—i.e., topography at the core-mantle boundary caused by flow and pressure from mantle convection, which reflects and sustains the mantle's internal structure (Wieczorek, 2015). Recently, Charalambous et al. (2025) presented evidence for kilometre-scale heterogeneities throughout Mars' mantle using seismic data from InSight. Kiefer et al. (1996) used long-wavelength topographic and gravity data to infer the mantle's thermal structure, revealing the presence of deep-seated anomalies. Their results highlight dominant contributions from spherical harmonic degrees 2 and 3.

As evident from any global image of Mars, and particularly from altimetry data, the northern hemisphere is lower than the southern hemisphere—a characteristic known as the Martian dichotomy (Zuber et al., 2000). This dichotomy is quantified by the degree-1 coefficient of Mars' surface topography. Mars is the only terrestrial planet exhibiting such a bi-phase terrain contrast. Recently, Goossens and Sabaka (2025) examined the degree-1 gravity associated with dichotomy, also clearly mentioned in Wieczorek et al. (2019), although they noted that the current resolution is insufficient for a robust determination of the corresponding large-scale density variations. Another distinctive feature of Mars is the presence of the vast Tharsis volcanic province, which has undergone prolonged volcanic activity over an extended period (Wieczorek, 2015). Zuber and Smith (1997) attempted to "remove" Tharsis from the Martian gravitational field in order to isolate its specific contributions. In doing so, they identified Tharsis as contributing primarily to degree-2, orders 0 and 2, as well as to degree-3, orders 0 and 3—although the latter components were found to be relatively small. Defraigne et al. (2001) proposed the presence of a mantle upwelling plume beneath Tharsis to explain the observed geoid anomaly. However, due to uncertainties in the observations, it remains impossible to discriminate between different mantle models that incorporate such a plume and its effects on core–mantle boundary (CMB) topography. In this study, we assume a solid mantle overlying the liquid core and disregard the possible existence of a basal liquid layer in the mantle, as suggested by Khan et al. (2023). Seismic data indicate that the Martian core is unusually large (Stähler et al., 2021), a result corroborated by radioscience

65   measurements (Le Maistre et al., 2023). In a core of this size, mantle pressures are insufficient to trigger a ringwoodite–
      bridgmanite phase transition in the lower mantle. Consequently, the predicted CMB topography is greater than in cases
      without a post-spinel phase transition, ranging from 1 km to 5 km. The impact of non-hydrostatic equilibrium at degree 2–
      order 0 of that level on the Free Core Nutation (FCN) was already highlighted in Defraigne et al. (2001). These results have
      motivated us to investigate the effects of CMB topography, expressed in spherical harmonics –particularly for degree-1,
70   degree-2, and degree-3– on the FCN, nutations, and LOD variations. Adding further interest to the liquid–solid boundary,
      Khan et al. (2023) and Samuel et al. (2024) recently showed that InSight data require the presence of a fully molten, ~150-
      km-thick silicate layer overlying the liquid iron core.

      As shown for the Earth (Puica et al., 2023; Dehant et al., 2025), the pressure torque acting on the CMB is proportional to the
      product of topography coefficients $\varepsilon_l^k \varepsilon_{l'}^{k'}$. It is therefore of second order in the topography, which additionally decreases with
75   increasing degree of the spherical harmonics (Kaula's law, see Puica et al., 2023). The pressure torque can therefore be
      expected to be small, in particular for higher spherical harmonic degrees. Nevertheless, the expression of the torque involves
      functions of inertial wave frequencies, which can lead to resonance effects when the tidal forcing frequency approaches the
      inertial wave frequency. These inertial waves, governed by the restoring effect of the Coriolis force, have periods of the
      order of weekly, diurnal, or sub-diurnal cycles and experience limited damping. As a result, they are strong candidates for
80   influencing nutations and short-period variations in LOD, provided a resonance effect occurs. This consideration has
      motivated us to analyse these cases through a spherical harmonic expansion of the topography up to degree 24, beyond
      which the topography amplitude becomes too small to affect observations, even near resonance.

      In our papers published in 2023 (Puica et al.) and in 2025 (Dehant et al.), we reviewed the state-of-the-art and discussed the
      literature available at that time. Since then, in a recent paper, Monville et al. (2025) presented topography-coupling
85   computations using local models of the CMB that incorporate rotation, buoyancy, and magnetic effects in a nonlinear
      regime. Due to the presence of both a magnetic field and stratification in the core, similarly as in the work of Seuren et al.
      (2025), their models include not only inertial waves but also Magneto-Archimedean-Coriolis (MAC) waves and Rossby
      waves. They compute the drag force exerted by core flows on the solid mantle and conclude that only large horizontal length
      scales contribute significantly to the CMB pressure torque. In our study, we focus exclusively on inertial waves (shorter
90   timescale), as Mars currently lacks an active magnetic field. In addition, Guervilly and Dormy (2025) conclude that core
      convection in the absence of a magnetic field is dominated by the inertial scale, which is hundred times larger than the
      viscous scale. Note that these studies neglect turbulence. In parallel, Oliver et al. (2025) show that turbulence in Earth's core
      can generate large topographic torques on the mantle—an effect not considered in the present work.

      In this paper, we compute the pressure effects exerted on the topography using an analytical approach to determine the
95   torque applied to the CMB. The general expression for this torque is presented in Section 1. We examine the impact on
      nutations in Section 2 and on LOD variations in Section 3. More precisely, *in Section 2*, we derive the analytical expression
      for the dynamic pressure amplitude, expanded in spherical harmonics, by considering the CMB flow boundary conditions
      (Subsection 2.1). The corresponding torque, also expressed analytically, depends on the topography coefficients developed

in spherical harmonics (Subsection 2.2). The nutation amplitudes are then derived from the coupling constant associated with

100 this torque (Subsection 2.3). We compare our results with those obtained for Earth in a recent study (Dehant et al., 2025) in the appendix of this paper. *In Section 3*, we analyse the LOD case, which is more straightforward, as the analytical expression for pressure takes a simpler form. We also compare our findings with those for Earth, as presented in a recent study by Puica et al. (2023). Finally, in Section 4, we present our conclusions.

1 Expression of the pressure torque on a bumpy core-mantle boundary

105 In the context of modelling Mars' orientation and rotational dynamics, the Liouville equations, which describe the conservation of angular momentum, form the theoretical foundation for quantifying how external torques—such as those from the atmosphere or solar tides— and internal torques between core and mantle affect the planet's spin axis orientation — nutations— and length-of-day variations (Wu and Wahr, 1997; Puica et al., 2023; Dehant et al., 2025). The presence of a pressure torque at the bumpy core-mantle boundary (CMB), $\boldsymbol{\Gamma^{topo}}$, introduces an additional term in the Liouville equations—

110 beyond the pressure contribution due to the core's hydrostatic flattening ($(\varepsilon_2^0)_{hydrostatic}$). To quantify this torque, the CMB radius is represented using a spherical harmonic expansion:

$$r_{CMB} = R\left[1 + \varepsilon_0^0 + (\varepsilon_2^0)_{hydrostatic}P_2^0(\cos\theta) + \sum_{n=1}^{\infty}\sum_{m=-n}^{n}\varepsilon_n^m Y_n^m(\theta,\lambda)\right] \qquad (1)$$

where ε_n^m are the coefficients of the CMB topography expansion, R is the mean CMB radius, and $Y_n^m(\theta,\lambda)$ are the fully normalized spherical harmonic functions, defined in terms of the fully normalized associated Legendre functions P_n^m by

115 $$Y_n^m(\theta,\lambda) = P_n^m(\cos\theta)e^{im\lambda} \qquad (2)$$

with (θ,λ) representing colatitude and longitude. Following Wu and Wahr (1997), we express the normalized dynamic pressure Φ as:

$$\Phi = \sum_{l=1}^{l_{max}} a_l^k\, P_l^k\left(\frac{\sigma}{2}\right) Y_l^k(\theta,\lambda) \qquad (3)$$

where σ is the frequency in a mantle-fixed reference frame, and the coefficients a_l^k are determined by using the boundary

120 conditions that relate the Poincaré motion (the main flow for nutations) or the global core faster or slower rotation with respect to the mantle (the main flow for LOD tidal effects) to the inertial waves. In our previous work for the Earth (Puica et al., 2023, for LOD; Dehant et al., 2025, for nutations), we employed a fully analytical approach, in contrast to Wu and Wahr (1997), who used a semi-analytical method.

For the nutation case, we consider the *x*- and *y*-components of the torque $\boldsymbol{\Gamma^{topo}}$ (Γ_1^{topo} and Γ_2^{topo}, respectively) on the diurnal

125 timescale. For Length-of-Day (LOD) variations, we focus on the *z*-component of the torque (Γ_3^{topo}). The equatorial torque components can be expressed as (Puica et al., 2023; Dehant et al., 2025)

$$\Gamma_1^{topo} = \left(-iA_f\Omega^2\right)\left(\frac{15}{8\pi}\right)^{\frac{1}{2}}\sum_{l=1}^{\infty}\sum_{k=-l}^{l}(-1)^k\left[\sqrt{l-k}\sqrt{l+k+1}\,\varepsilon_l^{-k-1} + \sqrt{l-k+1}\sqrt{l+k}\,\varepsilon_l^{-k+1}\right]P_l^k\left(\frac{\sigma}{2}\right)a_l^k \tag{4}$$

$$\Gamma_2^{topo} = \left(A_f\Omega^2\right)\left(\frac{15}{8\pi}\right)^{\frac{1}{2}}\sum_{l=1}^{\infty}\sum_{k=-l}^{l}(-1)^k\left[-\sqrt{l-k}\sqrt{l+k+1}\,\varepsilon_l^{-k-1} + \sqrt{l-k+1}\sqrt{l+k}\,\varepsilon_l^{-k+1}\right]P_l^k\left(\frac{\sigma}{2}\right)a_l^k \tag{5}$$

or in a complex form as

130 $$\Gamma_1^{topo} + i\,\Gamma_2^{topo} = \left(-iA_f\Omega^2\right)\left(\frac{15}{8\pi}\right)\sum_{l=1}^{\infty}\sum_{k=-l}^{l}(-1)^k\left[\sqrt{l-k}\sqrt{l+k+1}\,\varepsilon_l^{-k-1}\right]P_l^k\left(\frac{\sigma}{2}\right)a_l^k. \tag{6}$$

The polar component can be expressed as

$$\Gamma_3^{topo} = \left(iA_f\Omega^2\right)\left(\frac{15}{8\pi}\right)^{\frac{1}{2}}\sum_{l=1}^{\infty}\sum_{k=-l}^{l}(-1)^k\,k\,\varepsilon_l^{-k}P_l^k\left(\frac{\sigma}{2}\right)a_l^k. \tag{7}$$

In these expressions, A_f is the mean core moment of inertia and Ω is the planet mean rotation frequency. The factor $\frac{15}{8\pi}$ is coming from the definition of Wu and Wahr of the torque, involving $\rho_f\Omega^2R^5$ where ρ_f is the core density.

135 In Eq. (6), the coefficients a_l^k are substituted by using boundary conditions that relate the Poincaré motion ($\boldsymbol{\omega}_f \times \boldsymbol{r}$) –where $\boldsymbol{r}$ denotes the position vector of a fluid particle and $\boldsymbol{\omega}_f$ represents the vectorial wobble of the core relative to the mantle (Sasao et al., 1980)– to the inertial waves induced by the bumpy core-mantle boundary (Greenspan, 1969). In Eq. (7), the coefficients a_l^k are substituted using the boundary conditions corresponding to the global core rotation relative to the mantle, with $\omega_{f3} = -\omega_3$, where ω_3 is the third (axial) component of the mantle's rotation. These boundary conditions are described

140 in detail in the Appendices A and B of Wu and Wahr (1997). Since the torque components (Eqs. (6) and (7)) are proportional to either $\varepsilon_l^{-k-1}a_l^k$ or $\varepsilon_l^{-k}a_l^k$, and the coefficients a_l^k themselves are proportional to the topography, the torque components exhibit a quadratic dependence on the topography.

2 Nutation case

2.1 Boundary conditions

145 In the nutation case, to first order in ε_n^m, the relevant boundary conditions (Wu and Wahr, 1997) involve the mantle wobble with a normalized amplitude m, the Poincaré wobble in the core, with a normalized amplitude m_f, as well as inertial waves of which the expression in spherical harmonics includes the coefficients a_l^k.

At first order, and in the absence of topography, the ratio between mantle and core wobble amplitudes is given by:

$$\frac{m}{m_f} = \frac{A_f}{A}\frac{\sigma_{FCN}+\Omega}{\sigma_{FCN}-\alpha\Omega} \approx \frac{A_f}{A}\sigma'_{FCN} \tag{8}$$

150 where σ_{FCN} and σ'_{FCN} are the FCN frequencies expressed in the mantle frame and inertial space, respectively. Here, α denotes the hydrodynamic flattening of the planet and A is the mean moment of inertia of the entire planet. This relation shows that m is approximately three orders of magnitude smaller than m_f and can be neglected in the boundary conditions.

As shown in Dehant et al. (2025, see their Eq. 17), the boundary condition can then be expressed at the first order as

$$\frac{2}{3}\left(\frac{\sqrt{4\pi}}{\sqrt{5}}Y_2^0 - 1\right)\sum_{l,k}[\dots]_l^k \, a_l^k \, Y_l^k = \left(-\frac{2}{3}\frac{\sqrt{4\pi}}{\sqrt{5}}Y_2^0\right)\left[\sqrt{\frac{2\pi}{15}}\left(1Y_0^0 + 3\sum_{n=1}\varepsilon_n^m Y_n^m\right)\left(\frac{\sigma^2+\sigma-2}{\sigma}Y_2^1 m_f^- + \frac{-\sigma^2+\sigma+2}{\sigma}Y_2^{-1}m_f^+\right) +\right.$$

$$\left.\sqrt{\frac{2\pi}{3}}\left(\frac{\sigma^2+\sigma-2}{\sigma}Y_1^1 m_f^- + \frac{-\sigma^2+\sigma+2}{\sigma}Y_1^{-1}m_f^+\right)\Psi\right] + \frac{2}{3}\sqrt{\frac{2\pi}{15}}\left(1Y_0^0 + 3\sum_{n=1}\varepsilon_n^m Y_n^m\right)\left(\frac{\sigma^2+\sigma-2}{\sigma}Y_2^1 m_f^- + \frac{-\sigma^2+\sigma+2}{\sigma}Y_2^{-1}m_f^+\right) +$$

$$\sqrt{\frac{2\pi}{15}}\left(\frac{\sigma+2}{2}Y_2^1 m_f^- + \frac{\sigma-2}{2}Y_2^{-1}m_f^+\right)\sum_{n=1}m\varepsilon_n^m Y_n^m + \sqrt{\frac{2\pi}{3}}\left(\frac{\sigma^2-2\sigma-8}{6\sigma}Y_1^1 m_f^- + \frac{-\sigma^2-2\sigma+8}{6\sigma}Y_1^{-1}m_f^+\right)\Psi \tag{9}$$

with

$$\Psi = \sum_{n=1}^{\infty}\sum_{m=-n}^{n}\varepsilon_n^m\left[\frac{n\sqrt{n-m+1}\sqrt{n+m+1}}{\sqrt{2n+1}\sqrt{2n+3}}Y_{n+1}^m - \frac{(n+1)\sqrt{n-m}\sqrt{n+m}}{\sqrt{2n+1}\sqrt{2n-1}}Y_{n-1}^m\right] \tag{10}$$

and

$$[\dots]_l^k = \left[kP_l^k\left(\frac{\sigma}{2}\right) - \left(\frac{4-\sigma^2}{4}\right)P'_l^k\left(\frac{\sigma}{2}\right)\right]. \tag{11}$$

Here, m_f^+ denotes the complex sum of the first two components of the normalized core wobble, while m_f^- represents their complex difference. Additionally, we have replaced $\sin^2\theta$ using the identity

$$\sin^2\theta = \frac{2}{3}\left(-\frac{\sqrt{4\pi}}{\sqrt{5}}Y_2^0 + 1\right). \tag{12}$$

In the above equations, the dimensionless frequency σ, expressed in cycles per day, is related to the nutation frequency σ'_n defined in inertial space and σ_n defined in a frame tied to the planet, by:

$$\sigma = 1 - \frac{\sigma'_n}{\Omega} = -\sigma_n. \tag{13}$$

Note that while a negative quasi-diurnal frequency would typically be used in the selected reference frame, we follow the convention of Wu and Wahr (1997) and adopt the opposite sign.

To solve Eq. (9), we begin by expanding the sums and products in the equation using properties of spherical harmonic properties, which involves Wigner symbols. We then project the resulting expressions onto a single spherical harmonic by multiplying by its complex conjugate and integrating over the sphere. Each projection results in an equation in which the right-hand side (RHS) contains combinations of topography coefficients $\varepsilon_l^{k\pm1}$, $\varepsilon_{l\pm2}^{k\pm1}$, and $\varepsilon_{l\pm4}^{k\pm1}$, while the left-hand side (LHS) consists of terms involving a_l^k and $a_{l\pm2}^k$. All these projections form a system of equation of the form

$$A_{nut}\left(a_l^k\right) = f\left(\varepsilon_l^{k\pm1}, \varepsilon_{l\pm2}^{k\pm1}, \varepsilon_{l\pm4}^{k\pm1}\right). \tag{14}$$

Eq. (14) can be resolved for the coefficients a_l^k by inverting the matrix A_{nut} on the LHS. In practice, however, the problem is more efficiently handled by partitioning the system of linear equations into multiple independent subsystems, each of which can be solved individually. However, for specific values of the frequency, the determinant of the matrix A_{nut} (or of

the matrices of the subsystems) may be null, indicating singularities corresponding to *resonances*. Although Mars has a different uniform rotation rate, the resonances determined for the Earth (Dehant et al., 2025, Table 2) can still be used as a
180 reference framework considering they are normalized by the Martian rotation Ω.

The impact on nutation of a given resonance depends on how closely its period aligns with the nutation periods of interest. For Mars, we have identified three such cases involving the primary nutations and no case for LOD.

2.1.1 Degree 2

Since we primarily focus on low degrees (providing the largest topography amplitudes), we first consider the degree-2
185 topography coefficients only. Eq. (14) then simplifies to 10 equations containing products of two or three spherical harmonics ($Y_2^{\pm2}Y_2^{\pm1}$, $Y_3^{\pm2}Y_1^{\pm1}$, $Y_2^0Y_2^{\pm2}Y_2^{\pm1}$, $Y_2^0Y_3^{\pm2}Y_1^{\pm1}$). Through the expression of a product of two spherical harmonics of degrees l_1 and l_2, and orders m_1 and m_2, as a sum of spherical harmonics with degrees ranging from $|l_1 - l_2|$ to $l_1 + l_2$, and orders $m_1 + m_2$ (see, for example, MacRobert, 1967), we obtain a sum involving the following spherical harmonics Y_2^1, Y_2^{-1}, $Y_4^1, Y_4^{-1}, Y_4^3, Y_4^{-3}, Y_6^1, Y_6^{-1}, Y_6^3, Y_6^{-3}$. The solutions of the 10 equations can be obtained by solving the four decoupled
190 subsystems. Two involving degrees 4 and 6 with either order 3 or -3, and two with degrees 2, 4, and 6 with either order 1 or -1. The solutions of these subsystems can be expressed as

$$\begin{pmatrix} a_2^1 \\ a_4^1 \\ a_6^1 \end{pmatrix} = \begin{pmatrix} \frac{-1}{14\,[\ldots]_2^1}\left(\frac{3\sigma^2+4\sigma-20}{\sigma}\right) \\ \frac{5\sqrt{6}}{42\,[\ldots]_4^1}\left(\frac{\sigma^2-\sigma-2}{\sigma}\right) \\ 0 \end{pmatrix} \varepsilon_2^2 m_f^+ + \begin{pmatrix} \frac{-\sqrt{6}}{28\,[\ldots]_2^1}\left(\frac{\sigma^2+8\sigma+1}{\sigma}\right) \\ \frac{5}{7\,[\ldots]_4^1}\left(\frac{-\sigma^2-\sigma+2}{\sigma}\right) \\ 0 \end{pmatrix} \varepsilon_2^0 m_f^- \tag{15a}$$

$$\begin{pmatrix} a_2^{-1} \\ a_4^{-1} \\ a_6^{-1} \end{pmatrix} = \begin{pmatrix} \frac{1}{14\,[\ldots]_2^{-1}}\left(\frac{3\sigma^2-4\sigma-20}{\sigma}\right) \\ \frac{-5\sqrt{6}}{42\,[\ldots]_4^{-1}}\left(\frac{\sigma^2+\sigma-2}{\sigma}\right) \\ 0 \end{pmatrix} \varepsilon_2^{-2} m_f^- + \begin{pmatrix} \frac{\sqrt{6}}{28\,[\ldots]_2^{-1}}\left(\frac{\sigma^2-8\sigma+12}{\sigma}\right) \\ \frac{5}{7\,[\ldots]_4^{-1}}\left(\frac{\sigma^2-\sigma-2}{\sigma}\right) \\ 0 \end{pmatrix} \varepsilon_2^0 m_f^+ \tag{15b}$$

$$\begin{pmatrix} a_4^3 \\ a_6^3 \end{pmatrix} = \begin{pmatrix} \frac{-5}{\sqrt{42}\,[\ldots]_4^3}\left(\frac{\sigma^2+\sigma-2}{\sigma}\right) \\ 0 \end{pmatrix} \varepsilon_2^2 m_f^- \tag{15c}$$

195 $$\begin{pmatrix} a_4^{-3} \\ a_6^{-3} \end{pmatrix} = \begin{pmatrix} \frac{-5}{\sqrt{42}\,[\ldots]_4^{-3}}\left(\frac{-\sigma^2+\sigma+2}{\sigma}\right) \\ 0 \end{pmatrix} \varepsilon_2^{-2} m_f^+ \tag{15d}$$

They show that, for each frequency, the a_l^k coefficients depend only on the degree-2, order-0 or ±2 components of the topography, as well as on the position of the core rotation axis relative to the mantle (denoted $m_f^{\pm}$). These coefficients exhibit resonances at frequencies corresponding to the zeros of the bracketed terms appearing in the denominators of the governing Eqs. (15). These frequencies are at -2, -1.708, -1, -0.820, -0.612, -0.5, 0, 0.5, 0.612, 0.820, 1, 1.708, 2. Only the
200 frequency of 0.820 cycles/day in the Martian reference frame, corresponding to a period of about 5.5 days in space, could

affect the nutations if resonant terms existed near that period. However, there is no nutation near that period (see Baland et al., 2020).

2.1.2 Degree 1

In the case of degree-1, we similarly get 13 solutions as follows:

205
$$a_1^0 = \frac{1}{[\dots]_1^0}\left(\frac{\sqrt{2}}{210}\right)\left\{\frac{32\sigma^2+11\sigma-106}{\sigma}\varepsilon_1^{-1}m_f^- + \frac{-32\ ^2+11\sigma+106}{\sigma}\varepsilon_1^1 m_f^+\right\} \tag{16a}$$

$$a_1^{\pm 1} = \frac{1}{[\dots]_1^{\pm 1}}\left(\frac{-\sqrt{2}}{2}\right)\frac{\pm 65\ \sigma^2+149\sigma\pm 38}{210}\varepsilon_1^0 m_f^{-/+} \tag{16b}$$

$$a_3^0 = \frac{1}{[\dots]_3^0}\left(\frac{-1}{5\sqrt{7}\sqrt{6}}\right)\left\{\frac{10\ ^2+7\sigma-26}{\sigma}\varepsilon_1^{-1}m_f^- + \frac{-10\sigma^2+7\sigma+26}{\sigma}\varepsilon_1^1 m_f^+\right\} \tag{16c}$$

$$a_3^{\pm 1} = \frac{1}{[\dots]_3^{\pm 1}}\left(\frac{-1}{30\sqrt{7}}\right)\left\{\frac{\pm 35\sigma^2+29\sigma\pm(-82)}{\sigma}\right\}\varepsilon_1^0 m_f^{-/+} \tag{16d}$$

$$a_3^{\pm 2} = \frac{1}{[\dots]_3^{\pm 2}}\frac{-11}{3\sqrt{7}\sqrt{5}}\left\{\frac{\pm\sigma^2+\sigma\pm(-2)}{\sigma}\right\}\varepsilon_1^1 m_f^{-/+} \tag{16e}$$

210
$$a_5^0 = \frac{1}{[\dots]_5^0}\left(\frac{4}{7\sqrt{11}\sqrt{6}}\right)\left\{\frac{\sigma^2+\sigma-2}{\sigma}\varepsilon_1^{-1}m_f^- + \frac{-\sigma^2+\sigma+2}{\sigma}\varepsilon_1^1 m_f^+\right\} \tag{16f}$$

$$a_5^{\pm 1} = \frac{1}{[\dots]_5^1}\left(\frac{4\sqrt{2}}{7\sqrt{5}\sqrt{11}}\right)\frac{\pm\sigma^2+\sigma\pm(-2)}{\sigma}\varepsilon_1^0 m_f^{-/+} \tag{16g}$$

$$a_5^{\pm 2} = \frac{1}{[\dots]_5^{\pm 2}}\frac{2}{\sqrt{5}\sqrt{7}\sqrt{11}}\frac{\pm\sigma^2+\sigma\pm(-2)}{\sigma}\varepsilon_1^1 m_f^{-/+} \tag{16h}$$

The a_l^k coefficients depend on the three degree-one topography coefficients and on the orientation of the rotation axis of the core. Here again, they exhibit resonances at frequencies corresponding to the zeros of the bracketed terms appearing in the
215 denominators of the governing Eqs. (16). These frequencies are at -2, -1.806, -1.530, -1.510, -1.496, -1.183, -1.046, -0.894, -0.763, -0.667, -0.570, -0.467, -0.177, -0.068, 0, 0.068, 0.177, 0.467, 0.570, 0.667, 0.763, 0.894, 1.046, 1.183, 1.496, 1.510, 1.530, 1.806, 2. Only the frequencies 0.894, 1.046, 1.183 cycle/day in the Martian frame, corresponding to periods near 9.4 days, -21.7 days, and -5.5 days in space, could have an effect on the nutations. There is no nutation near these periods.

2.1.3 Other degrees

220 Also in the general case, the solutions for $a_l^{\pm k}$ exhibit resonances, determined by the roots of the corresponding $[\dots]_l^{\pm k}$. Table 1 presents these resonances, along with the degree l and order k of the spherical harmonics where they occur, as well as the nearby nutation frequency.

225   Table 1. Principal resonances close to Martian nutations.

Nutation period in Martian days			Degree and order (l,k)	Inertial wave resonance period	Difference between nutation period and inertial wave period
-111.430	1/6 year	retrograde	(12, 6)	-102.493	8.937
-111.430	1/6 year	retrograde	(24, -4)	-109.392	2.038
-167.150	1/4 year	retrograde	(18, -12)	-157.218	9.932
-222.866	1/3 year	retrograde	(12, -2)	-206.826	16.040
-334.300	0,5 year	retrograde	(16, -5)	-262.304	71.996
133.720	1/5 year	prograde	(21, -2)	135.876	2.156
133.720	1/5 year	prograde	(21, 6)	138.412	4.692
133.720	1/5 year	prograde	(24, -2)	125.853	7.867
133.720	1/5 year	prograde	(24, 6)	126.088	7.632
133.720	1/5 year	prograde	(23, -8)	148.036	14.316
167.150	1/4 year	prograde	(14, -6)	163.739	3.411
167.150	1/4 year	prograde	(23, -8)	148.036	19.114
167.150	1/4 year	prograde	(18, -2)	168.602	1.453
167.150	1/4 year	prograde	(18, 6)	182.895	15.745
167.150	1/4 year	prograde	(19, 9)	171.142	3.992
334.300	0,5 year	prograde	(21, 13)	274.074	60.226
334.300	0,5 year	prograde	(15, -2)	370.692	36.393
668.599	1 year	prograde	(15, 6)	793.770	125.171
668.599	1 year	prograde	(20, 15)	937.350	268.751
668.599	1 year	prograde	(23, 12)	1004.721	336.121

Table 1 shows that the nutation closest to an inertial wave is the quarter-annual nutation, which is 1.4 days away from an inertial wave period.

2.2 Expression of the torque at the core-mantle boundary

The torque associated with the topography $\tilde{\Gamma}_{topo}(\sigma)$ is expressed by Eqs. (4), (5) and (6) proportional to ε_l^{-k-1} or ε_l^{-k} and
230   involving the normalized inertial pressure, Φ provided by Eq. (3), acting on the boundary bumps, which involves the normal to the CMB topography, as explained above in Section 1. As done in Dehant et al. (2025), we just need to substitute a_l^k as a function of ε_n^m (except for degree 2, order 1) to obtain the final expression of the torque.

For the topography coefficients ε_n^m, we adopt a generalized Kaula law, as supported by Puica et al. (2023). With this assumption, the CMB topography coefficients decrease with increasing spherical harmonic degree. The dominant
235   contributions to $\tilde{\Gamma}_{topo}(\sigma)$ on Mars are likely associated with dynamic topography driven by the mantle's internal structure, which is also reflected in surface gravity anomalies. As shown in Defraigne et al. (2001), the effect of mantle mass anomalies differs between the geoid and the CMB topography: the low-degree geoid is most sensitive to anomalies at depths of about 700 km, whereas the CMB topography is primarily sensitive to anomalies near the CMB, at approximately 1830 km depth. This relationship is encapsulated by the Green's function—i.e., the kernel that links mantle mass anomalies to
240   surface/geoid or CMB topography—derived in Defraigne et al. (2001). Using the observed geoid together with these Green's

functions, and assuming that the amplitudes of mantle loads is independent of depth (but varies with the degree and order of each gravity coefficient), we can estimate the order of magnitude of the corresponding CMB topography. These amplitudes scale with the Martian gravity field coefficients, all listed in Table 2.

Table 2. Main Mars gravity field coefficients.

Topography coefficients expressed as sine (s) and cosine (c) components relevant for Tharsis	Normalized Mars gravity field coefficients amplitudes (Zuber and Smith, 1997; Smith et al., 1993) (*10^{-6} and above 10^{-5})	Order of magnitude of the CMB topography contribution (m)
ε_2^0	**-44**	**400**
ε_{c2}^1 & ε_{s2}^1 (or equivalently ε_2^{-1} & ε_2^1)	0.004 & 0.007	
ε_{c2}^2 & ε_{s2}^2 (or equivalently ε_2^{-2} & ε_2^2)	**84 & 50**	**760 & 450**
ε_3^0	-12	250
ε_{c3}^1 & ε_{s3}^1 (or equivalently ε_3^{-1} & ε_3^1)	4 & 25	65 & 390
ε_{c3}^2 & ε_{s3}^2 (or equivalently ε_3^{-2} & ε_3^2)	16 & 8	250 & 125
ε_{c3}^3 & ε_{s3}^3 (or equivalently ε_3^{-3} & ε_3^3)	35 & 25	550 & 390
ε_{c4}^4 & ε_{s4}^4 (or equivalently ε_4^{-4} & ε_4^4)	0.1 & -13	2 & 330

245

The chosen CMB topography includes in fact a contribution from the Tharsis mass anomaly, which is predominantly represented by degree-2, order-2 terms, followed by degree-2, order-0, and then degree-3, order-3 components, in decreasing order of amplitude. As shown in Table 2, the degree-2 terms are the most significant. Other components (such as ε_3^0, ε_3^{-1}, ε_3^1, ε_3^{-2}, ε_3^2, ε_4^{-4} and ε_4^4) are smaller than the degree-2 terms. Due to Mars' hemispheric dichotomy, the topography may also

250   contain a significant degree-1 component, which we will account for in the following analysis.

2.2.1 Degree 2

For the a_l^k involving degree-2 spherical harmonics, the torque expression (1) yields:

$$\tilde{\Gamma}^{topo} = \Gamma_1^{topo} + i\,\Gamma_2^{topo} = (-iA\Omega^2)\left(\frac{15}{8\pi}\right)\left\{\varepsilon_2^0 P_2^{-1}\left(\frac{\sigma}{2}\right)a_2^{-1} + \varepsilon_2^{-2}P_2^1\left(\frac{\sigma}{2}\right)a_2^1 + \varepsilon_4^0 P_4^{-1}\left(\frac{\sigma}{2}\right)a_4^{-1} + \varepsilon_4^{-2}P_4^1\left(\frac{\sigma}{2}\right)a_4^1\right\} \qquad (17)$$

After substituting Equations (15) for the a_l^k, we obtain:

255
$$\tilde{\Gamma}^{topo} = (-iA\Omega^2)\left(\frac{15}{8\pi}\right)\left\{\frac{1}{16}\sigma(4-\sigma^2)^{1/2}\left\{\frac{1}{14\,[...]_2^{-1}}\left(\frac{3\sigma^2-4\sigma-2}{\sigma}\right)\varepsilon_2^0\varepsilon_2^{-2}\boldsymbol{m}_f^- + \frac{\sqrt{6}}{28\,[...]_2^{-1}}\left(\frac{\sigma^2-8\sigma+1}{\sigma}\right)\varepsilon_2^0\varepsilon_2^0\boldsymbol{m}_f^+\right\} + \frac{-3}{8}\sigma(4-$$

$$\sigma^2)^{1/2}\left\{\frac{-1}{14\,[...]_2^1}\left(\frac{3\sigma^2+4\sigma-20}{\sigma}\right)\varepsilon_2^{-2}\varepsilon_2^2\boldsymbol{m}_f^+ + \frac{-\sqrt{6}}{28\,[...]_2^1}\left(\frac{\sigma^2+8\sigma+1}{\sigma}\right)\varepsilon_2^0\varepsilon_2^{-2}\boldsymbol{m}_f^-\right\} + \frac{1}{128}(7\sigma^3-12\sigma)\;(4-$$

$$\sigma^2)^{1/2}\left\{\frac{-5\sqrt{6}}{42\,[...]_4^{-1}}\left(\frac{\sigma^2+\sigma-2}{\sigma}\right)\varepsilon_4^0\varepsilon_2^2\boldsymbol{m}_f^+ + \frac{5}{7\,[...]_4^{-1}}\left(\frac{\sigma^2-\sigma-2}{\sigma}\right)\varepsilon_4^0\varepsilon_2^0\boldsymbol{m}_f^+\right\} + \frac{-5}{32}\;(7\sigma^3-12\sigma)(4-$$

$$\sigma^2)^{1/2}\left\{\frac{5\sqrt{6}}{42\,[...]_4^1}\left(\frac{\sigma^2-\sigma-2}{\sigma}\right)\varepsilon_4^{-2}\varepsilon_2^2\boldsymbol{m}_f^+ + \frac{5}{7\,[...]_4^1}\left(\frac{-\sigma^2-\sigma+2}{\sigma}\right)\varepsilon_4^2\varepsilon_2^0\boldsymbol{m}_f^+\right\}\right\}. \tag{18}$$

where the brackets $[...]_{2/4}^{\pm 1}$ are obtained from Eq. (11).

260 **2.2.2 Degree 1**

For the a_l^k involving degree-1 spherical harmonics the torque expression (6) can be expressed considering the topographic coefficients relevant to both the dichotomy and Tharsis, and substituting the expressions for P_l^k and a_l^k, involving $[...]_l^k$:

$$\tilde{\Gamma}^{topo} = \Gamma_1^{topo} + i\,\Gamma_2^{topo} = (-iA\Omega^2)\left(\frac{15}{8\pi}\right)\left\{\left(\frac{-1}{210}\right)\frac{65\sigma^2+149\sigma+38}{\sigma-2}\varepsilon_1^0\varepsilon_1^0 m_f^+ + \left(\frac{2}{105}\right)\frac{32\sigma^2+11\sigma-106}{\sigma^2-4}\varepsilon_1^{-1}m_f^- +$$

$$\left(\frac{-2}{105}\right)\frac{32\sigma^2-11\sigma-106}{\sigma^2-4}\varepsilon_1^1 m_f^+ + \left(\frac{-2}{\sqrt{7}}\frac{\sqrt{2}}{\sqrt{15}}\right)\frac{\sigma^2+\sigma-2}{3\sigma^2-4\sigma+4}\varepsilon_3^{-3}\varepsilon_1^{-1}m_f^+\right\} \tag{19}$$

265 where the roots of $\sigma-2$, σ^2-4, and $3\sigma^2-4\sigma+4$ provide resonances. Nothing appears in the nutation frequency band.

2.3 Effects on nutations

The transfer function for nutations can be derived from the transfer function for the mantle wobble $\tilde{m}$ of Mars defined as the complex sum of the two first components of the non-dimensional rotation axis coordinates ($m_1 + i\,m_2$). The wobbles, $\tilde{m}$ and $\tilde{m}_f$, of the mantle and the core (with $\tilde{m}_f = m_{f1} + i\,m_{f2}$), respectively, are solutions to the Liouville equations. We

270 distinguish between the case without topography (denoted as $\tilde{m}^0$ and $\tilde{m}_f^0$), and the case with a topography at the CMB. The additional contribution to the mantle wobble due to the topography (Dehant et al., 2025) is proportional to the topographic torque, as computed in the previous section or in Section 1 (Eq. (6)), according to

$$\tilde{m} = \tilde{m}^0 - i\,\frac{\sigma_n}{\sigma_n-\sigma_{nFCN}}\frac{\tilde{\Gamma}_{topo}}{A_m\Omega^2} \tag{20}$$

where σ_n is the nutation frequency as introduced above (Eq. (13)), σ_{nFCN} is the FCN frequency, and A_m is the mean mantle

275 moment of inertia. The associated nutation contribution $\Delta\tilde{\eta}_n$ can be determined from the nutation transfer function given by Eq. (1) from Dehant et al. (2025):

$$\Delta\tilde{\eta}_n(\sigma_n) = \tilde{\eta}_n - \tilde{\eta}_n^0 = \tilde{\eta}_n^0\left(\frac{-\sigma_n}{\Omega_0(\sigma_n-\sigma_{nFCN})(A\sigma_n-A_m\sigma_{nFCN})}\frac{A}{A_m}\frac{i\tilde{\Gamma}_{topo}(\sigma)}{m_f^+(\sigma)}\right) \tag{21}$$

where $\tilde{\eta}_n$ is the complex sum of the rotation pole first-two components expressing nutations in space and where the superscript 0 indicates the values when there is no topography. For the highest degrees, since the topographic torque depends on the square of the small topography coefficients, significant contributions can only occur in the vicinity of resonances. Figure 1 displays the determinant of the matrix A_{nut} in Eq. (14) (up to degree 24) to be inverted. Values equal to zero indicate the frequencies at which resonances can occur for nutations.

◆	1 year prograde	◆	1 year retrograde	+	1/2 year prograde
+	1/2 year retrograde	★	1/3 year prograde	★	1/3 year retrograde
■	1/4 year prograde	■	1/4 year retrograde	●	1/5 year prograde
●	1/5 year retrograde	◇	1/6 year prograde	◇	1/6 year retrograde
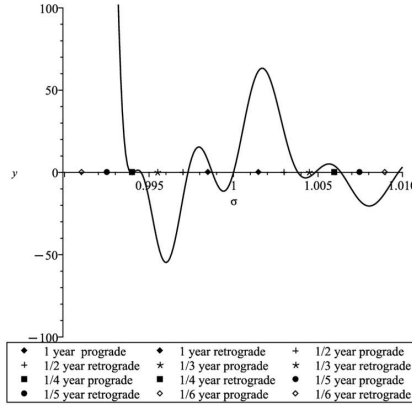
Figure 1: Determinant of the matrix A_{nut} involved in the system of equations (14), showing the resonances where the curve is crossing zero. The nutation periods are shown with the symbols in the caption.

In Section 2.2.1, we have provided, as an example, the degree-2 contributions to the torque, where we observe some resonance effects when the nutation frequencies are close to the frequencies corresponding to brackets $[...]_{2/4}^{\pm 1}$ close to 0. Figure 1 shows the results for all degrees. For the primary nutations of Mars, we have identified three possible resonances (see Table 1):

(1) **First resonance**: This occurs in the solution for a_{24}^{-4}, appearing at approximately -109.39 Martian days, close to the 1/6-year retrograde nutation at -111.43 Martian days. However, this nutation has a very small amplitude of 20 microarcseconds (µas) (see Rosenbergh and Kink, 1979; Baland et al., 2020), and the resonance is 2.0 Martian days away from it. As a result, the computed topography effect remains below the microsecond level.

(2) **Second resonance**: This appears in the solution for a_{21}^{-2} at 135.88 Martian days, near the 1/5-year prograde nutation at 133.72 Martian days. In this case as well, the amplitude is very small at 2.8 milliarcseconds (mas), and the resonance is 2.1 days away from the nutation. Consequently, the effect remains well below the microsecond level.

(3) **Third resonance**: This occurs in the solution for a_{18}^{-2}, appearing at approximately 168.60 Martian days, close to the 1/4-year prograde nutation at 167.15 Martian days. While its amplitude is 18.4 mas, its period is still more than 1 day from the resonance, and the associated topography is extremely small (as for the two other cases), resulting in an effect at the microarcsecond level.

In conclusion, the forced nutation frequencies are insufficiently close to any resonant frequency to have a significant effect on the nutation (not even at the microsecond level).

3 Length-of-day variations

The effects of CMB topography on the tidal variations in LOD can be calculated using a similar approach to that described

305 above (Puica et al. 2023). For LOD, and analogously to the boundary conditions for nutations (Eqs. (9) and (14)), we have a system of equations of the form:

$$\mathbf{A_{LOD}}(a_l^k) = f(\varepsilon_l^k) \quad (22)$$

where each equation for a particular order l and degree k involves a bracket $[...]_l^k$ on the LHS and a function of ε_l^k on the RHS. The solutions yield expressions for the coefficients a_l^k given in Eq. (28) of Puica et al. (2023). The zeros of the

310 determinant of the matrix $\mathbf{A_{LOD}}$, which correspond to the zeros of the $[...]_l^k$ brackets, indicate resonance effects.

We then substitute the solution of Eq. (22) for a_l^k into the expression for the torque, which is in turn substituted into the expression of the tidal variations in LOD, $\Delta LOD(\sigma)$. Finally, the LOD variations can be expressed as a function of the axial component of the mantle wobble, m_3:

$$\Delta LOD(\sigma) = -i\frac{\Gamma_3}{A_m \sigma \Omega^2} = \frac{A_f}{A_m}\left(\frac{15}{8\pi}\right)\left(\sum_{l=1}^{l_{max}}\sum_{k=-l}^{l}(-1)^k k^2 \varepsilon_l^k \varepsilon_l^{-k} P_l^k\left(\frac{\sigma}{2}\right)\frac{(4-\sigma^2)}{4\sigma\,[...]_l^k}m_3\right) \quad (23)$$

315 where the product $\varepsilon_l^k \varepsilon_l^{-k}$ clearly shows the quadratic dependence of the LOD on the topography. Resonances occur only when the denominator term $[...]_l^k = 0$. Figure 2 shows the determinant of the matrix A_{LOD}. As in Figure 1 (nutation-case), the presence of resonances in LOD is indicated when the curve crosses the zero line.
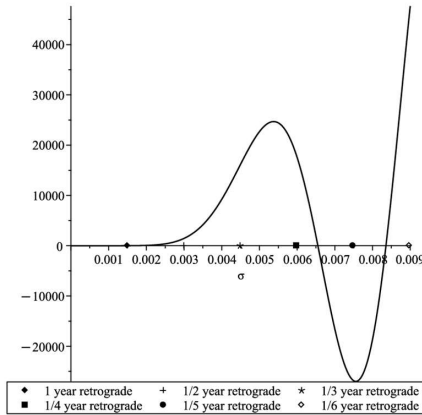
Figure 2: Determinant of the matrix A_{LOD} involved in the system of equations (22), showing the resonances where the curve is
320 **crossing zero. The LOD seasonal periods are shown with the symbols in the caption.**

As shown in Figure 2 there are no resonances close to the Martian tidal frequencies of 668.6, 334.3, 222.9, 167.15, 133.7, and 111.4 Martian days. The nearest periods to a resonance are the 1/6-year and 1/5-year tides, which are approximately 7.1 and 7.9 days away from an inertial wave resonance, respectively. These distances are too large to produce significant

resonant effects, particularly given that the associated spherical harmonic degrees (15 and 22) correspond to extremely small

325   topographic coefficients (ε_{15}^{-1} and ε_{22}^{-2}). In contrast, for Earth, several tidal periods shorter than one month lead to resonances near the 13.63-day and 27.6-day tides (see Puica et al., 2023).

4 Conclusions

Following our previous studies on topographic effects on Earth's LOD and nutations—where potential resonance effects with inertial waves were demonstrated—we applied our analytical framework to planet Mars. The existence of core modes within

330   Mars is plausible, as its core has been shown to be liquid. In the absence of a significant magnetic field, these modes are essentially inertial waves, with the Coriolis force acting as the primary restoring mechanism.

In our model, we considered primary a possible degree-1 topography related to Mars' hemispheric dichotomy, as well as low-degree topographic features potentially associated with the dynamic loading from the Tharsis region at the CMB. We also considered higher degree effects through a Kaula-law extrapolation of the topography.

335   Our analysis of Martian nutations reveals a potential resonance at 168.60 Martian days, which lies close to the 1/4-year prograde nutation period at 167.15 Martian days— differing by just over one day. This nutation exhibits an amplitude of 18.4 mas, which is significant at the level of radioscience observations. However, despite this proximity, the actual topography contribution to nutation remains negligible, as the resonance involves a high degree (degree-18) and therefore small topographic amplitude.

340   Unlike Earth, where LOD variations can be significantly influenced by low-degree CMB topography, Mars shows no comparable resonant effects near its tidal periods. As a result, we find no evidence of substantial inertial wave resonance contributing to LOD variations on Mars. Generally speaking, in our analytical case, we found a quadratic dependence on the topography amplitude, both for Earth and Mars. As a result, the effects of CMB coupling are generally small, unless resonances occur.

345   Our study does not consider the effect of turbulence at the CMB. Using numerical simulations of hydrodynamic convection in a rotating spherical shell with boundary topography, Oliver et al. (2025) recently showed that turbulent flow in the core of the Earth can lead to a pressure torque on that mantle of sufficient magnitude to explain LOD variations. These results indicate a linear dependence of the topographic torque on the CMB topography. However, it should be noted that the torque acting on the CMB is proportional to the square of the flow speed. The flow speed considered for Earth is associated with the

350   geodynamo and core convection, processes that are absent in Mars.

Appendix

Visual comparison of Earth and Mars nutations

355
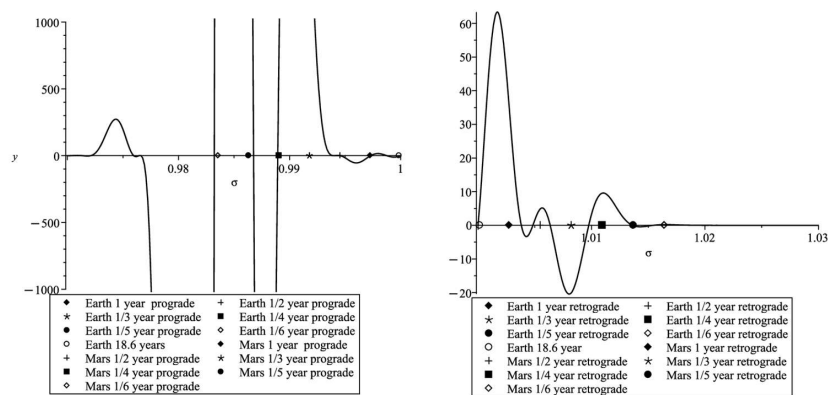
Figure A1: Determinant of the matrix A_{nut} involved in the system of equations (14), showing the resonances where the curve is crossing zero. The prograde part is shown on the left and the retrograde part, on the right. The nutation periods are shown with the symbols in the caption.

360

Author contribution

MF and VD developed the analytical approach and computed the resonances and topographic torque. MP developed the initial Maple code used for the resonance computations. TVH provided expertise in the geophysical interpretation of the results.

365 ## Competing interests

The contact author has declared that none of the authors has any competing interests.

Financial support

The research leading to these results has received funding from the European Research Council under ERC synergy grant 855677 (GRACEFUL - Gravimetry, magnetism and core flow) under the European Union's Horizon 2020 research and innovation programme. Also the Belgian Fund for Scientific Research FNRS-FRS is acknowledged for its financial support through the research project number PDR T.0066.20 at UCLouvain.

References

Baland, R. M., Yseboodt, M., Le Maistre, S., Rivoldini, A., Van Hoolst, T., Dehant, V.: The precession and nutations of a rigid Mars, Celest. Mech. Dyn. Astr., 132, 47, doi:10.1007/s10569-020-09986-0, 2020.

Banerdt, W. B., Smrekar, S., Banfield, D., Giardini, D., Golombek, M., Johnson, C., Lognonné, P., Spiga, A., Spohn, T., Perrin, C., Stähler, S., Antonangeli, D., Asmar, S., Beghein, C., Bowles, N., Bozdag, E., Chi, P., Christensen, U., Clinton, J, Collins, G., Daubar, I., Dehant, V., Drilleau, M., Fillingim, M., Folkner, W., Garcia, R., Garvin, J, Grant, J, Grott, M., Grygorczuk, J, Hudson, T., Irving, J, Kargl, G., Kawamura, T., Kedar, S., King, S., Knapmeyer-Endrun, B., Knapmeyer, M., Lemmon, M., Lorenz, R., Maki, J, Margerin, L., McLennan, S., Michaut, C., Mimoun, D., Mittelholz, A., Mocquet, A., Morgan, P., Mueller, N., Murdoch, N., Nagihara, S., Newman, C., Nimmo, F., Panning, M., Pike, W., Plesa, A. C., Rodriguez, S., Rodriguez-Manfredi, J, Russell, C., Schmerr, N., Siegler, M., Stanley, S., Stutzmann, E., Teanby, N., Tromp, J, van Driel, M., Warner, N., Weber, R., Wieczorek, M.: Initial results from the InSight mission on Mars, Nature Geoscience, 13, 183–189, doi:10.1038/s41561-020-0544-y, 2020.

Charalambous, C., Pike, W. T., Kim, D., Samuel, H., Fernando, B., Bill, C., Lognonné, P.: Seismic evidence for a highly heterogeneous martian mantle, Science, 389, 899–903, doi:10.1126/science.adk4292, 2025.

Defraigne, P., Dehant, V., Van Hoolst, T.: Steady-state convection in Mars' mantle, Planet. Space Sci., 49, 501–509, 2001.

Dehant, V., Van Hoolst, T., and Defraigne, P.: Comparison between the nutations of the planet Mars and the nutations of the Earth, Survey Geophys., 21, 1, pp. 89–110, doi:10.1023/A:1006716529241, 2000.

Dehant, V., Folkner, W., Renotte, E., Orban, D., Asmar, S., Balmino, G., Barriot, J. P., Benoist, J, Biancale, R., Biele, J, Budnik, F., Burger, S., de Viron, O., Häusler, B., Karatekin Ö., Le Maistre, S., Lognonné, P., Menvielle, M., Mitrovic, M., Pätzold, M., Rivoldini, A., Rosenblatt, P., Schubert, G., Spohn, T., Tortora, P., Van Hoolst, T., Witasse, O., and Yseboodt, M.: Lander Radioscience for obtaining the rotation and orientation of Mars, Planet. Space Sci., 57, pp. 1050–1067, doi:10.1016/j.pss.2008.08.009, 2009.

Dehant, V., Le Maistre, S., Rivoldini, A., Yseboodt, M., Rosenblatt, P., Van Hoolst, T., Mitrovic, M., Karatekin Ö., Marty, J. C., and Chicarro, A.: Revealing Mars' deep interior: Future geodesy missions using radio links between landers, orbiters, and the Earth, Planet. Space Sci., Special Issue on 'Comparative Planetology: Venus-Earth-Mars', 59(10), pp. 1069–1081, doi:10.1016/j.pss.2010.03.014, 2011.

Dehant, V., Banerdt, B., Lognonné, P., Grott, M., Asmar, S., Biele, J, Breuer, D., Forget, F., Jaumann, R., Johnson, C., Knapmeyer, M., Lefeuvre, M., Mimoun, D., Mocquet, A., Read, P., Rivoldini, A., Romberg, O., Schubert, G., Smrekar, S., Spohn, T., Tortora, P., Ulamec, S., Vennerstrøm, S.: Future Mars geophysical observatories for understanding its internal structure, rotation, and evolution, Planet. Space Sci., 68(1), 123–145, doi:10.1016/j.pss.2011.10.016, 2012.

Dehant, V., Puica, M., Folgueira, M., Rekier, J, Trinh, A., Van Hoolst, T.: Analytical computation of the total topographic torque at the Core-Mantle Boundary and its impact on nutations, Geophys. J. Int., 241, 474–494, doi:10.1093/gji/ggaf050, 2025.

405 Drilleau, M., Samuel, H., Rivoldini, A., Panning, M., Lognonné, P.: Bayesian inversion of the Martian structure using geodynamic constraints, Geophysical Journal International, 226(3), 1615–1644, doi:10.1093/gji/ggab105, 2021.

Drilleau, M., Samuel, H., Garcia, R. F., Rivoldini, A., Perrin, C., Wieczorek, M., Lognonné, P., Banerdt, W. B.: Constraints on lateral variations of Martian crustal thickness from seismological and gravity field measurements, Geophysical Research Letters, 51, e2023GL105701, doi:10.1029/2023GL105701, 2024.

410 Goossens, S., Sabaka, T. J.: Probing Lateral Density Variations in the Crust from Gravity and Topography: Applications to the Moon and Mars, The Planetary Science Journal, 6(3), 71, doi:10.3847/PSJ/adbaf0, 2025.

Greenspan, H. P.: The Theory of Rotating Fluids, Cambridge University Press, ISBN 10: 0521051479, ISBN 13: 9780521051477, 1969.

Guervilly, C., Dormy, E.: The cross-over from viscous to inertial lengthscales in rapidly-rotating convection, Geophysical 415 Research Letters, 52, e2024GL111593, doi:10.1029/2024GL111593, 2025.

Khan, A., Ceylan, S., Van Driel, M., Giardini, D., et al.: Upper mantle structure of Mars from InSight seismic data, Science, 373, 434–438, DOI:10.1126/science.abf2966, 2021.

Khan, A., Huang, D., Durán, C. et al.: Evidence for a liquid silicate layer atop the Martian core, Nature, 622, 718–723, doi:10.1038/s41586-023-06586-4, 2023.

420 Kiefer, W. S., Bills, B. G., Nerem, R. S.: An inversion of gravity and topography for mantle and crustal structure on Mars, J. Geophys. Res. Planets, 101, 9239–9252, doi:10.1029/95JE03699, 1996.

Konopliv, A. S., Park, R. S., Folkner, W. M.: An improved JPL Mars gravity field and orientation from Mars orbiter and lander tracking data, Icarus, 274, 253–260, doi:10.1016/j.icarus.2016.02.052, 2016.

Le Maistre, S., Caldiero, A., Rivoldini, A., Yseboodt, M., Baland, R. M., Beuthe, M., Van Hoolst, T., Dehant, V., Folkner, 425 W. M., Buccino, D., Kahan, D., Marty, J. C., Antonangeli, D., Badro, J, Drilleau, M., Konopliv, A., Péters, M. J., Plesa, A. C., Samuel, H., Tosi, N., Wieczorek, M., Lognonné, P., Panning, M., Smrekar, S., Banerdt, W. B.: Spin state and deep interior structure of Mars from InSight radio tracking, Nature, 619(7971), 733–737, doi:10.1038/s41586-023-06150-0, 2023.

MacRobert, T. M.: Spherical Harmonics: An Elementary Treatise on Harmonic Functions with Applications, Pergamon Press, ISBN 10: 0080121152, ISBN 13: 9780080121154, 1967.

430 Monville, R., Cébron, D., Jault, D.: Topographic drag at the core-mantle interface, Journal of Geophysical Research: Solid Earth, 130, e2024JB029770, doi:10.1029/2024JB029770, 2025.

Oliver, T. G., Blackman, E. G., Tarduno, J. A., Calkins, M. A.: Turbulence in Earth's core generates large topographic torques on the mantle, ArXiv, arXiv:2410.19934 [physics.geo-ph], 25 pp., doi:10.48550/arXiv.2410.19934; Commun Earth Environ, 6, 484, doi:10.1038/s43247-025-02451-6, 2025.

435 Puica, M., Dehant, V., Folgueira, M., Van Hoolst, T., Rekier, J: Analytical computation of the total topographic torque at the Core-Mantle Boundary and its impact on tidally driven Length-of-Day variations, Geophys. J. Int., 234(1), 585–596, doi:10.1093/gji/ggad077, 2023.

Reasenberg, R. D., King, R. W. (1979) The rotation of Mars, J. Geophys. Res., 84, 6231–6240, doi:10.1029/JB084iB11p06231.

440 Samuel, H., Drilleau, M., Rivoldini, A., Xu, Z., Huang, Q., Garcia, R. F., Lekić, V., Irving, J. C. E., Badro, J, Lognonné, P. H., Connolly, J. A. D., Kawamura, T., Gudkova, T., Banerdt, W. B.: Geophysical evidence for an enriched molten silicate layer above Mars's core, Nature, 622, 712–717, doi:10.1038/s41586-023-06601-8, 2023.

Sasao, T., Okubo, S., Saito, M.: A simple theory on the dynamic effects of a stratified fluid core upon nutational motion of the Earth, In: "Nutation and the Earth's rotation", Proc. IAU Symposium, Kiev, Ukrainian SSR 1977, Dordrecht, D. Reidel 445 Publishing Co., pp. 165–183, 1980.

Seuren, F., Triana, S. A., Rekier, J, Dehant, V., Van Hoolst, T.: The influence of a stably stratified layer on the hydromagnetic waves propagating in the Earth's fluid outer core and their electromagnetic torques, Geophys. J. Int., accepted, 2025.

Smith, D. E., Lerch, F. J., Nerem, R. S., Zuber, M. T., Patel, G. B., Fricke, S. K., Lemoine, F. G.: An improved gravity 450 model for Mars: Goddard Mars Model 1, Journal of Geophysical Research, 98(E11), 20871–20890, doi:10.1029/93JE01839, 1993.

Smith, D. E., Sjogren, W. L., Tyler, G. L., Balmino, G., Lemoine, F. G., and Konopliv, A. S.: The Gravity Field of Mars: Results from Mars Global Surveyor, Science, 286(5437), 94–97, doi:10.1126/science.286.5437.94, 1999.

Stähler, S. C., Khan, A., Banerdt, W. B., Lognonné, P., Giardini, D., Ceylan, S., Drilleau, M., Duran, A. C., Garcia, R. F., et 455 al.: Seismic detection of the martian core, Science, 373,443–448, doi:10.1126/science.abi7730, 2021.

Wieczorek, M. A.: Gravity and Topography of the Terrestrial Planets, In: Treatise on Geophysics (Second Edition), Volume 10, 153–193, doi:10.1016/B978-0-444-53802-4.00169-X, 2015.

Wieczorek, M. A., Beuthe, M., Rivoldini, A., Van Hoolst, T.: Hydrostatic interfaces in bodies with nonhydrostatic lithospheres, J. Geophys. Res. Planets, 124, 1410–1432, 2019.

460 Wu, X., Wahr, J. M.: Effects of non-hydrostatic core-mantle boundary topography and core dynamics on Earth rotation, Geophys. J. Int., 128(1), 18–42, doi:10.1111/j.1365-246X.1997.tb04069.x, 1997.

Zuber, M. T., Smith, D. E.: Mars without Tharsis, J. Geophys. Res., 102(E12), 28673–28685, doi:10.1029/97JE02527, 1997.

Zuber, M. T., et al.: Internal Structure and Early Thermal Evolution of Mars from Mars Global Surveyor Topography and Gravity, Science, 287,1788–1793, doi:10.1126/science.287.5459.1788, 2000.